

pubs.acs.org/JPCC Article

Mechanisms of Degradation of Na₂Ni[Fe(CN)₆] Functional Electrodes in Aqueous Media: A Combined Theoretical and Experimental Study

Xaver Lamprecht, Iman Evazzade, Iago Ungerer, Ludek Hromadko, Jan M. Macak, Aliaksandr S. Bandarenka,* and Vitaly Alexandrov*



Cite This: J. Phys. Chem. C 2023, 127, 2204-2214



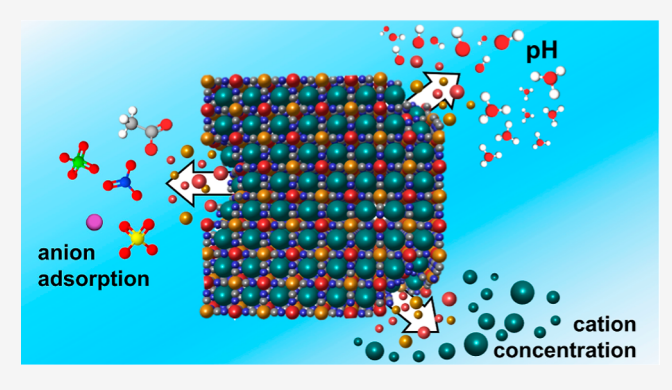
ACCESS

III Metrics & More

Article Recommendations

s Supporting Information

ABSTRACT: Prussian blue analogues (PBAs) are versatile functional materials with numerous applications ranging from electrocatalysis and batteries to sensors and electrochromic devices. Their electrochemical performance involving long-term cycling stability strongly depends on the electrolyte composition. In this work, we use density functional theory calculations and experiments to elucidate the mechanisms of degradation of model Na₂Ni[Fe(CN)₆] functional electrodes in aqueous electrolytes. Next to the solution pH and cation concentration, we identify anion adsorption as a major driving force for electrode dissolution. Notably, the nature of adsorbed anions can control the mass and charge transfer mechanisms during metal cation intercalation as well as the electrode degradation rate. We find that weakly



adsorbing anions, such as NO_3^{-} , impede the degradation, while strongly adsorbing anions, such as SO_4^{2-} , accelerate it. The results of this study provide practical guidelines for electrolyte optimization and can likely be extrapolated to the whole family of PBAs operating in aqueous media.

INTRODUCTION

Prussian blue analogues (PBAs) are widely used in different materials science disciplines as they provide various functionalities for battery applications, ¹⁻⁵ (electro)sensorics, ⁶⁻⁸ heterogeneous (electro)catalysis, ⁹⁻¹¹ desalination and selective ion removal, ^{12–14} as well as electrochromic devices. ^{15,16} PBAs can be represented by the general formula A_xTM¹[TM²(CN)₆], where A is usually Li, Na, or K, and TM is a transition metal such as Fe, Mn, Cu, Co, Ni, or Zn. The transition metals are interconnected by C≡N bridges forming TM(CN)₆ octahedra, which creates an open framework structure with A-site cations occupying the interstitial nanopores. These cations can be reversibly inserted and extracted from an electrolyte (which will be used synonymously with the term "intercalation" throughout this report) and diffuse through the three-dimensional channels in the structure.4 Typically, PBAs are associated with the facecentered cubic lattice, but the monoclinic and rhombohedral structures are also commonly observed due to symmetry distortions such as octahedral tilts, Jahn-Teller distortions, hexacyanometallate vacancies, or framework hydration. 17,18 Owing to the high tunability of chemical composition, PBAs can be considered as model materials in coordination and inorganic chemistry, being analogues of the well-known metal-organic frameworks (MOFs). 19 Therefore, a basic understanding of the correlations between various functional

properties of PBAs and their composition or structure is of great fundamental importance.

In the case of energy conversion and storage applications, the properties of electrified interfaces between electronically conducting PBAs and aqueous electrolytes are of central significance. So far, one fundamental property that has received very limited attention is the electrochemical stability of PBAbased electrodes. Most of the previous stability studies focused on how solution pH affects the degradation of PBA materials: it was found that PBAs are prone to degradation in both acidic (low pH)²⁰⁻²⁴ and basic (high pH) solutions.^{20,25-28} However, it was recently demonstrated that the degradation rate of aqueous sodium-ion battery electrodes based on PBAs strongly depends not only on solution pH but also on the nature of anions present in the electrolytes.²⁹ Specifically, for the Na₂Ni[Fe(CN)₆] and Na₂Co[Fe(CN)₆] model electrodes, the transition-metal dissolution during charge-discharge cycles was monitored in real time using an electrochemical flow-cell linked with an inductively coupled plasma mass

Received: November 23, 2022 Revised: January 16, 2023 Published: January 30, 2023





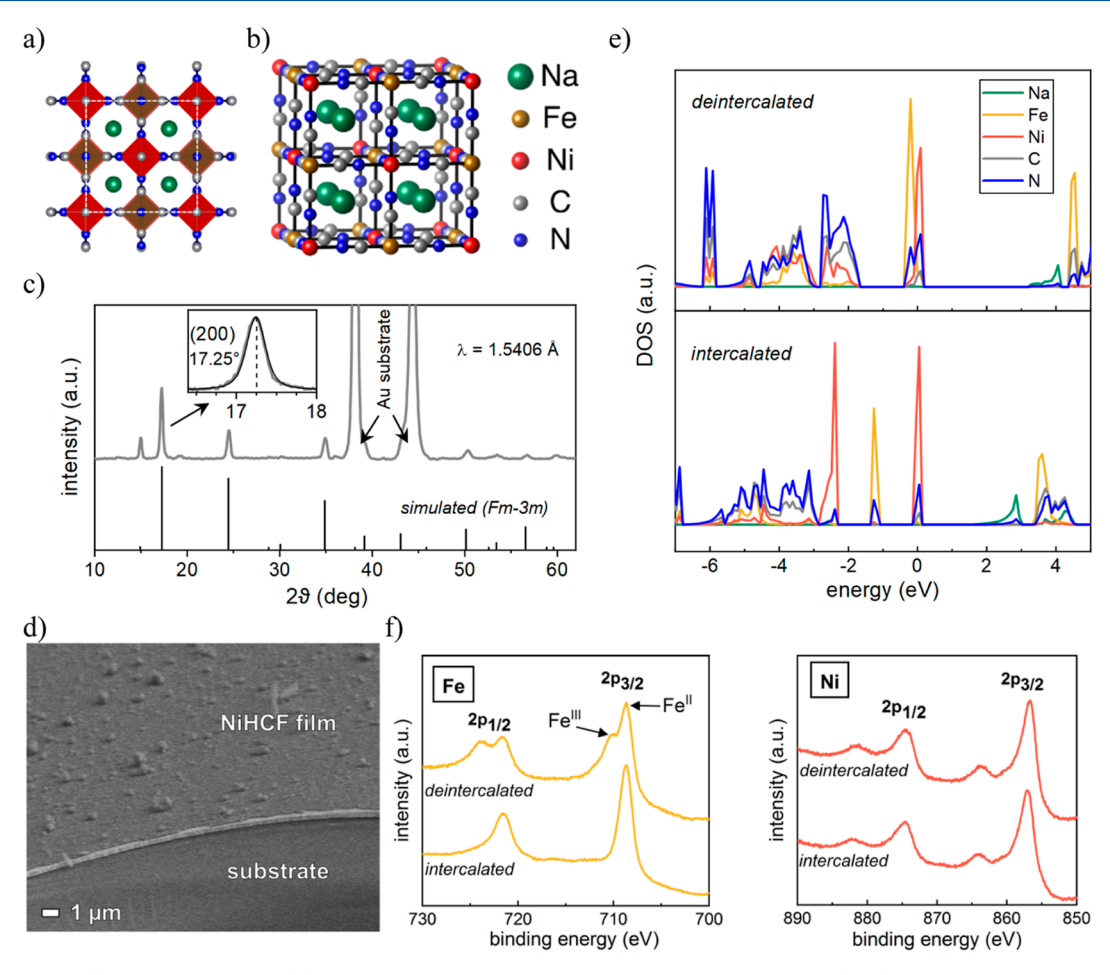


Figure 1. Polyhedral (a) and ball-and-stick (b) representations of the nickel hexacyanoferrate $Na_2Ni[Fe(CN)_6]$ crystal structure in the cubic space group $Fm\overline{3}m$. (c) XRD pattern of the NiHCF thin film together with the simulated reflections for the crystal structure given in (b). SEM image of the electrodeposited thin-film electrode (d). (e) DOS for fully intercalated and 50% deintercalated bulk NiHCF. (f) XPS spectra showing the Fe 2p and Ni 2p regions for intercalated and deintercalated NiHCF.

spectrometer. The study revealed distinct transition-metal dissolution patterns strongly correlated with the electrochemical potential and current. It was shown that the degradation rate increases in the order ${\rm ClO_4}^- < {\rm NO_3}^- < {\rm Cl}^- < {\rm SO_4}^{2-}$, revealing almost no capacity loss after 10,000 cycles for ${\rm Na_2Ni[Fe(CN)_6]}$ in highly concentrated NaClO₄. However, the atomistic mechanisms underlying such behavior remain unclear.

In this work, we combine experiments and density functional theory calculations to elucidate the properties of the electrified interface between model nickel hexacyanoferrate {NiHCF, Na₂Ni[Fe(CN)₆], and NaNi[Fe(CN)₆]} electrodes and aqueous electrolytes in the presence of anions commonly used in electrochemical systems. A significant affinity of the PBA surface to anionic species explains the complex mechanism of the interfacial mass and charge transfer during intercalation of alkali metal cations and drastic differences in the stability of PBA materials in the presence of different anions. 30-32 It is found that surface Fe-sites are more favorable for anion adsorption than Ni-sites. Toward the edges of the pH scale, the initial stages of the electrode degradation involve the attack of Fe-sites by OH⁻ (at high pH) or protonation of the CN groups of the crystal (at low pH) via intercalated H₃O⁺. These findings should be of great importance for optimizing the electrochemical behavior of PBA-containing systems,

interpreting experimental results, and refinement of advanced models of the electrified PBA/electrolyte interfaces.

METHODS

Experimental Section. Electrochemical experiments were performed in an electrochemical glass cell under inert argon (Ar 5.0, Westfalen) atmosphere in a three-electrode configuration. 1.37 cm² AT-cut Au quartz crystal wafers (Stanford Research Systems, Ti adhesive layer, 5 MHz) served as substrates for the electrochemical deposition of NiHCF thin films to monitor the mass loading and variation via electrochemical quartz crystal microbalance (EQCM). A platinum wire was used as a counter electrode, and an Ag/AgCl reference electrode (SSC, 3 M KCl, SI Analytics, "B 3420+") was used. All measurements were performed using a Bio-Logic VSP-300 potentiostat.

The synthesis of $Na_2Ni[Fe(CN)_6]$ model electrodes was performed by means of cyclic voltammetry with a scan rate of 50 mV/s in an aqueous solution of 0.25 M Na_2SO_4 (\geq 99%, Sigma-Aldrich), 0.5 mM $K_3[Fe(CN)_6]$ (99%, Sigma-Aldrich), and 0.5 mM $NiCl_2$ (99.3%, Alfa Aesar). The deposition method is further described in refs 2931, and 32.

The electrochemical characteristics and stability of NiHCF were investigated in different Na^+ electrolytes as shown in Table S1. The electrolytes and precursor solutions were prepared with ultrapure water (18.2 M Ω , Merck Millipore).

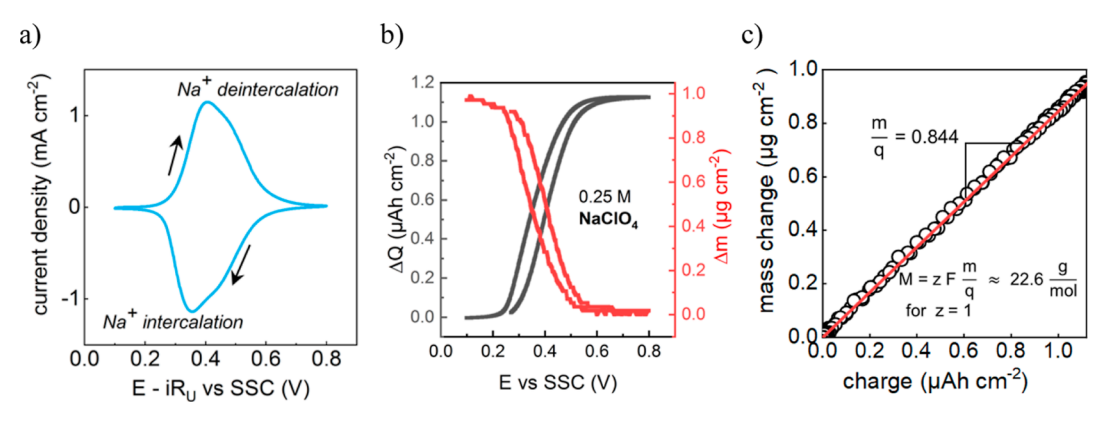


Figure 2. (a) Representative cyclic voltammogram of NiHCF in 0.25 M NaClO₄ showing the redox response of Fe^{II/III} in the PBA complex. The electrode charge and mass change (b) during the forward and backward scan of the CV are correlated to Na⁺ (de)intercalation by EQCM using Faraday's law (c).

Cyclic voltammograms were recorded with a scan rate of 50 mV/s and galvanostatic cycling (0.1-0.8 V vs SSC) was performed with a rate of 300 C, whereas 1 C generally corresponds to a (dis)charging time of 1 h. Impedance spectra were recorded at a constant potential of 0.4 V vs SSC, which equals a degree of sodiation of approximately 60%. The amplitude of the probing signal was set to 10 mV, and the scanned frequency range was between 35 kHz and 1 Hz with 10 points per decade in logarithmic spacing. All electrolytes were tested in the order of NaClO₄, NaNO₃, NaCl, Na₂SO₄, and NaCH3COO on the same sample with an unchanged electrode setup for good comparability of the results with minimal degradation between the measurements. The stationarity of the system was ensured by an appropriate waiting period before the measurement and the validity of all spectra was guaranteed by the Kramers-Kronig check (see Figure S1). The data were fitted to an electrical equivalent circuit using the software EIS Data Analysis 1.3.33

To study the crystallographic properties of the NiHCF thin film, grazing incidence X-ray diffraction (XRD) analysis was carried out in the range of $2\theta = 5-65^{\circ}$ (step size = 0.026°) using Panalytical Empyrean with a Cu tube ($\bar{\lambda} = 1.5406$ Å, 45 kV, 40 mA) and Pixcel3D detector. The incident angle was 1°. The software VESTA (version 3.0)³⁴ was used to visualize crystal structures and simulate the diffraction pattern of Na₂Ni[Fe(CN)₆], implying a face-centered cubic space group $(Fm\overline{3}m)$ crystal structure with a lattice constant of 10.28 Å. A field-emission scanning electron microscope (SEM, JSM-7500F, JEOL) was used to characterize the thin-film electrode morphology. The elemental composition and electronic binding energies of NiHCF samples were investigated by Xray photoelectron spectroscopy (XPS, Specs). The X-ray source was an Al K-alpha anode (1486.61 eV, 12 kV, 200 W) and photoelectrons were detected with a PHOIBOS 150 2D CCD detector.

Computational Details. All spin-polarized density functional theory (DFT) plane-wave calculations are performed using the Vienna Ab initio Simulation Package (VASP). The revised Perdew-Burke-Ernzerhof (RPBE) generalized gradient approach (GGA) functional is employed in combination with the on-site Hubbard U parameters ($U_{\rm Fe}=3.3~{\rm eV}$ and $U_{\rm Ni}=4.6~{\rm eV}$) and ferromagnetic ordering following previous theoretical investigations. The D3 approach within Grimme's formalism is applied to correct for van der Waals interactions. The core electrons are represented

through the projector augmented-wave (PAW) formalism. 41 A plane-wave cutoff energy of 500 eV is used throughout the 5 is employed for the bulk and 5 \times 5 \times 1 for the slab calculations. Structural optimizations are carried out until the total energies and atomic forces are converged to within 10⁻⁵ eV and 0.05 eV/Å, respectively. During structural optimizations, the bottom half of the slab is kept fixed. The optimized lattice constant of $Na_2Ni[Fe(CN)_6]$ is 10.32 Å. The dimensions of the used periodic slabs are $10.32 \times 10.32 \times$ 10.32 Å³ with at least a 15 Å vacuum gap. For the optimized adsorption configurations, an additional single-point calculation within the implicit solvent model is performed using the default relative permittivity of the bulk water (78.4). The calculations are carried out for both the fully intercalated $Na_2Ni[Fe(CN)_6]$ and 50% deintercalated $NaNi[Fe(CN)_6]$ slabs, which correspond to eight Na species in the former case and four Na species in the bottom layer of the slab in the latter case, respectively.

■ RESULTS AND DISCUSSION

Figure 1a,b shows the atomic structure of nickel hexacyanoferrate $\{Na_2Ni[Fe(CN)_6]\}$ used in this study as a representative PBA to better understand its degradation properties in aqueous electrolytes. The recorded XRD pattern of the electrodeposited thin film (see Figure 1c) matches very well with the calculated pattern for the $Fm\overline{3}m$ structure. The strong (200) reflection allows us to calculate the lattice constant for the material yielding 10.28 Å. This value is in good accordance with the results of our DFT optimization (10.32 Å). It is, therefore, reasonable to use the presented atomic structure for further DFT simulations of the processes at the electrified electrode–electrolyte interface. As visible from the SEM image in Figure 1d, the NiHCF thin film obtained from the electrochemical deposition is characterized by a very homogenous coating on top of the Au substrate.

The electrochemical activity in PBAs is based on alkali metal ions, for example, sodium, (de)intercalation accompanied by the corresponding redox reaction of the host transition metals. NiHCF has only Fe(II/III) as an active redox center since Ni species are electrochemically inert in the operating window of water-based electrolytes. The corresponding redox reaction is represented by

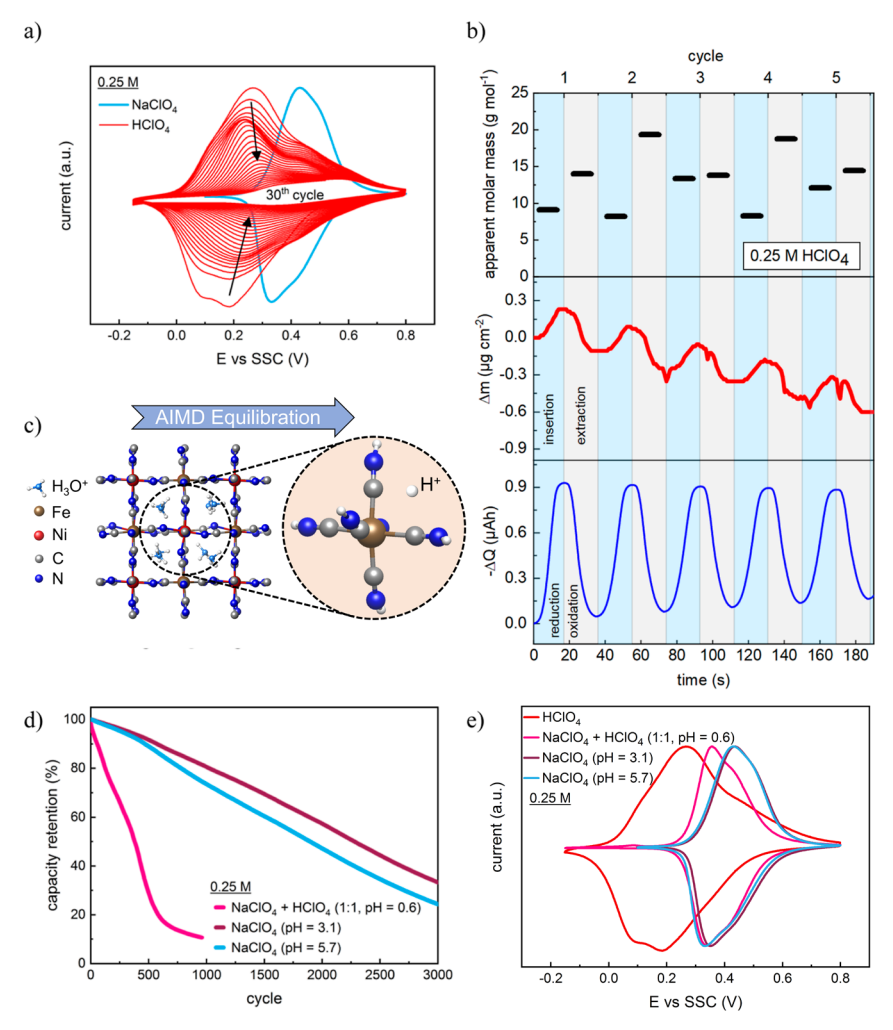


Figure 3. (a) Fast degradation of NiHCF in 0.25 M HClO₄ during voltametric cycling due to active material dissolution. (b) Correlation of the corresponding charge and mass change as measured via EQCM over the first five CV cycles. The apparent molar mass of the intercalate was calculated from $\Delta m/\Delta Q$ using Faraday's law. The ongoing electrode dissolution causes large fluctuations in the obtained molar mass values. (c) Ab initio molecular dynamics simulation predicts the cleavage of the $[Fe-C \equiv N]-Ni$ bond due to protonation of the N-sites if Na⁺ in NiHCF is replaced by H₃O⁺. (d) Impact of the H⁺ vs Na⁺ availability on the stability of NiHCF during galvanostatic cycling and (e) respective CVs.

$$Na_2Ni^{II}[Fe^{II}(CN)_6]$$
 (intercalated)

$$\Rightarrow Na^+ + e^- + NaNi^{II}[Fe^{III}(CN)_6]$$
(50% deintercalated) (1)

Indeed, our Bader charge analysis based on DFT calculations of the NiHCF slabs shows that Ni ions do not change their charge upon 50% deintercalation with q(Ni) = 1.30, whereas the positive charge on Fe ions increases from q(Fe) = 1.17 for the fully intercalated case up to 1.33 for the deintercalated case. This agrees well with an analysis of the density of states (DOS), revealing that the Fe electronic states below the Fermi energy for the intercalated material shift toward the Fermi level for the deintercalated material (Figure 1e). We note here that the analysis based on Bader charges can only be considered qualitative.

This is further confirmed by XPS measurements of oxidized and reduced electrodes, which were electrochemically brought to their respective final states. NiHCF was completely reduced at a potential of 0.1 V vs SSC, whereas it was completely oxidized at 0.8 V vs SSC. As seen in Figure 1f, the samples show strongly differing spectra in the Fe 2p region. For the intercalated electrode, one sharp peak, which is observed in

both regions of the spin—orbit doublet, can be associated with the Fe^{II} oxidation state as expected for fully sodiated NiHCF. Upon deintercalation, Fe^{II} is oxidized to Fe^{III}, which is well represented by the appearance of an additional peak at higher binding energies in both doublet regions. On the other side, the spectra obtained for Ni 2p show identical peaks with regard to the corresponding binding energies and intensities, proving that Ni is electrochemically inert within the investigated potential window.

The electrochemical oxidation (desodiation) and reduction (sodiation) of the NiHCF electrode in 0.25 M NaClO₄ result in a reversible redox peak (see Figure 2a). It can be noted that the CV peak comprises a superposition of two sharp peaks at $\sim\!0.38$ and $\sim\!0.46$ V versus SSC. This double-peak structure results from the formation of two different stoichiometries of NiHCF during the electrodeposition process {Na₂Ni^{II}[Fe^{II}(CN)₆] and NaNi_{1.5}^{II}[Fe^{II}(CN)₆]}, whereas Fe(II/III) remains the redox-active center in both cases. ^43-45 For simplicity, this work considers NiHCF as the former stoichiometry. The electrode mass change over one CV cycle, as measured by EQCM, strictly follows the consumed charge (Figure 2b). By using Faraday's law, a molar mass of 22.6 g mol⁻¹ is obtained for the (de)intercalating species, from

which it can be confirmed that the charge compensation is achieved by the transport of Na⁺ ions across the electrode–electrolyte interface (Figure 2c).

It was previously reported that the transition-metal dissolution from NiHCF is highly dependent on solution pH and anions present in the electrolyte. ²⁹ However, the NiHCF degradation mechanism as a function of electrolyte composition remains poorly understood. This study distinguishes two degradation regimes corresponding to acidic and alkaline aqueous electrolytes.

We first analyze the mechanism of active material degradation in acidic solutions in the absence of alkali metal cations. It can be assumed that at low pH, the most abundant cationic solution species available for intercalation into the NiHCF structure are hydronium (H₃O⁺) ions. An oxidized NaNi[Fe(CN)₆] electrode was transferred to a 0.25 M HClO₄ solution and electrochemically cycled in the absence of Na⁺ in the electrolyte (Figure 3a). Starting right from the first cycle, the material degrades severely, as visible from the rapidly decreasing current waves in the voltammogram. After less than 30 cycles, the redox activity has almost entirely vanished. Similarly, an instantaneous degradation was observed for desodiated NiHCF in 0.25 M H₂SO₄, which can be considered as completely degraded after already 20 cycles (Figure S2a). It should be noted that the potential range was extended toward lower potentials, as the redox peak was shifted for the acidic solutions compared to the Na+ electrolytes. It has been reported that the nature of the intercalating cationic species strongly impacts the insertion potential (E_i) of PBA materials, with E_i decreasing when going up the periodic table from the large Cs⁺ ion toward the small Li⁺. This correlation generally results from the fact that the insertion potential is thermodynamically linked to the Gibbs free energy of solvation, which decreases with increasing ionic radii of the intercalate. 46-49 It is, therefore, reasonable that the intercalation of H₃O⁺ in NiHCF is observed at potentials lower than that of Na+.

To first prove that hydronium is indeed inserted into and extracted from NiHCF, Figure 3b shows the variation in the electrode mass as measured by EQCM during voltametric scans in 0.25 M HClO₄. A continuous mass loss indicates the dissolution of the electrode, which reflects the diminishing redox response in Figure 3a. This is overlaid with a repetitive mass increase and decrease signal, which is characteristic of the insertion of ionic species into a host electrode from the solution. By applying Faraday's law, the apparent molar mass of the intercalate is obtained between 8.2 and 19.4 g mol⁻¹. It should be noted that the large fluctuation of this value is caused by the superposition of the (de)insertion signal with the electrode dissolution, as well as the noisy EQCM data caused by the harsh degradation process. Similar results with apparent molar masses between 9.4 and 21.9 g mol⁻¹ were obtained for NiHCF in 0.25 M H₂SO₄ (see Figure S2b). Even though the respective average molar masses are smaller than the expected 19 g mol⁻¹ for H₃O⁺, the data undoubtedly prove the intercalation and deintercalation of a cationic species associated with the reduction and oxidation of NiHCF in the HClO₄ and H₂SO₄ solutions. This finding strongly indicates that hydronium actively participates in the (de)intercalation

Due to the highly decreased cycling stability of NiHCF in the $\mathrm{Na^+}$ -free acidic solutions compared to pH-neutral $\mathrm{Na^+}$ electrolytes, it can be assumed that the intercalation of $\mathrm{H_3O^+}$ is

likely responsible for the fast structure destruction. To probe the acidic dissolution mechanism by a theoretical approach, we replace Na⁺ cations in the NiHCF structure with H₃O⁺, maintaining the same charge of the cell, and run the ab initio molecular dynamics (AIMD) simulations. Already after 1-2 ps of AIMD equilibration, we observed spontaneous protonation of the N-sites resulting in the generation of Fe(CN-H)₆ moieties (see Figure 3c). This suggests that the N-sites are the primary point of attack in acidic electrolytes during the NiHCF degradation process. This should lead to the dissolution of Fe(CN)₆³⁻ complexes, while the remaining Ni cations are expected to dissolve as solvated Ni²⁺ species. ²⁹ It was reported that highly defective copper hexacyanoferrate (CuHCF, a Turnbull's blue analogue) can operate as a stable and reversible proton insertion electrode in 2 M H₂SO₄, whereas the stability deteriorated strongly when replacing Cu by Ni, Co, or Mn.⁵ Our AIMD simulations predicted a similar protonation of Nsites for CuHCF, which contrasts the reported stability of this system. We hypothesize that the high content of coordination water within the defective CuHCF lattice may effectively prevent N-sites from rapid protonation, and therefore, that a high degree of crystal hydration may allow a more stable proton insertion into PBAs.

Considering this, one could erroneously conclude that the presence of $\rm H_3O^+$ in general has a detrimental impact on PBA electrodes in aqueous media. However, acidification of alkali metal cation electrolytes is, overall, a well-established strategy to enhance the stability of PBAs. ^{29,51,52} The reason for its higher stability in slightly acidified electrolytes is usually assigned to the absence of OH⁻, as it is well-known that PBA electrodes are entirely unstable in the presence of abundant hydroxide species. ^{26–28} Figure S3 shows the almost immediate disintegration of NiHCF upon cycling in 0.1 M NaOH (pH = 13). As previously reported, the electrode degradation at high pH is characterized by an entire loss of $[Fe(CN)_6]^{3/4-}$ and the subsequent formation of surface-confined NiO $_x$ phases, represented by the increasing current from the Ni(II/III) redox couple. ^{27–29}

This stabilization strategy based on OH- removal is represented in Figure 3d, where the reduction in the pH of a $NaClO_4$ solution from its initial value of pH = 5.7 to pH = 3.1 via the addition of HClO₄ leads to a significant decrease in the degradation rate during the galvanostatic cycling. If the electrolyte is, however, strongly acidified with an equal concentration of 0.25 M HClO₄ and NaClO₄, the NiHCF electrode degradation is extremely accelerated, whereas it is still more stable compared to the pure 0.25 M HClO₄ solution (Figure 3a). For both cases of acidified electrolytes, we assign the charge compensation mechanism mainly to the intercalation of Na⁺ rather than H₃O⁺. This is reflected by the respective CVs shown in Figure 3e. As the intercalation potential E_i of NiHCF for sodium is higher than that for protons in the pure NaClO₄ and HClO₄ solutions at equal concentrations, it can be deduced that sodium insertion is in general thermodynamically more favored. 47-49 For the pHadjusted 0.25 M NaClO₄ electrolyte (pH = 3.1), the CV exactly resembles the one for the pH = 5.7 electrolyte. Furthermore, an apparent molar mass of ~ 23 g mol⁻¹ was found for the intercalating species, which shows that Na⁺ is responsible for the charge compensation even in acidified electrolytes (see Figure S4). For the 0.25 M HClO₄ and NaClO₄ (1:1) mixed solution, the CV appears at a lower potential than for the pure 0.25 M NaClO₄ case. As the total

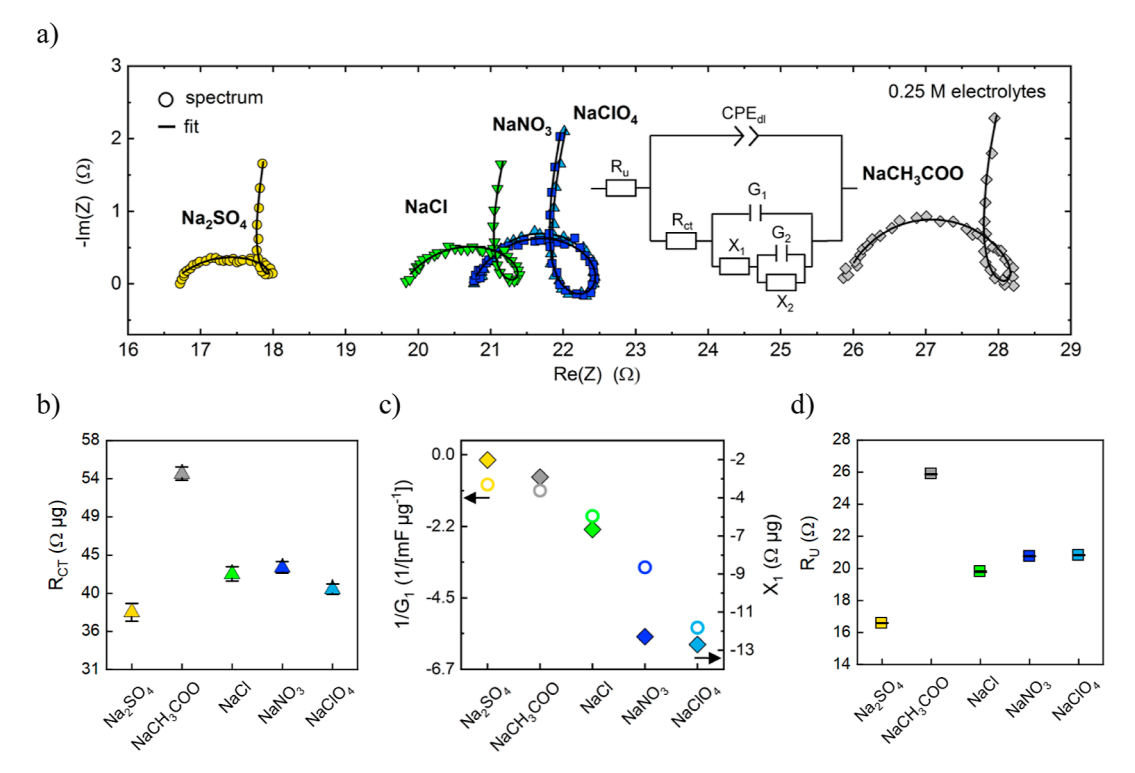


Figure 4. (a) Impedance spectra (at 0.4 V vs SSC) of NiHCF recorded in 0.25 M Na⁺ electrolytes with varying anion species. The impedance spectra were fitted using the displayed equivalent circuit yielding the extracted fitting parameters for $R_{\rm CT}$ (b), $1/G_1$ (hollow symbols, left axis) with X_1 (filled symbols, right axis) (c), and R_n (d).

 $\mathrm{Na^{+}}$ concentration is only 0.125 M, this behavior is well described by the relation 49,53

$$E_{\rm i} = E_{\rm A}^0 + \frac{RT}{F} \ln \frac{c_{\rm A}}{c_0} \tag{2}$$

where E_A^0 is the standard potential of the cation intercalation reaction with c_A , the cation concentration in the solution, and c_0 , the reference concentration at which E_A^0 is evaluated. R is the universal gas constant, T is the absolute temperature, and Fis the Faraday constant. According to eq 2, a shift of the insertion potential of 18 mV to the left is expected for a Na⁺ concentration of 0.125 M vs the original 0.25 M solution. The experimentally obtained shift of the insertion potential is ~30 mV, which can be explained by a coinsertion of H₃O⁺ to a small extent. This is, furthermore, reflected by the apparent molar mass of the intercalating species, which was obtained as \sim 21.2 g mol⁻¹ (see Figure S5). It has been reported that the insertion of two cationic species A and B in PBAs results in a single CV peak, with its E_i being between the two extrema $E_{i,A}$ and $E_{i,B}$. The resulting position of E_i indicates the dominating intercalate of A and B, confirming that Na+ is the main intercalating species even in a 1:1 mixed Na⁺/H₃O⁺ solution. However, it appears striking that the CV shape of NiHCF exhibits a much lower peak-to-peak separation when a high concentration of hydronium is present, which might be caused by the extremely fast kinetics associated with proton $insertion. \\^{50}$

Considering the obtained stability trend, the apparent molar masses, and the CV peak positions of the Na^+/H^+ mixed solutions, we conclude that NiHCF has a higher affinity for Na^+ insertion compared to H_3O^+ , and the stabilization is caused by the reduced coinsertion of hydronium when Na^+ ions are available as an intercalate. Therefore, the use of

slightly acidified Na^+ electrolytes (to $pH \approx 3$) should serve as a very effective strategy to enhance the stability of PBA electrodes due to the practical absence of OH^- while still providing a high Na^+/H_3O^+ ratio.

For alkaline/neutral solutions, we investigate the role of a series of common anionic species on the degradation rate of PBA materials. We have shown in our previous studies that electrolyte anions play a significant role in the interfacial charge and mass transfer processes for intercalation-type battery materials.30-32,54Figure 4a shows the impedance spectra for NiHCF in 0.25 M Na⁺ electrolytes for varying anions, in particular, ClO₄-, NO₃-, Cl-, CH₃COO-, and SO₄²⁻. Characteristic loop-shaped spectra were obtained for all the electrolytes, which were fitted with the equivalent electric circuit displayed in Figure 4a. Next to the "classical" elements as the uncompensated resistance (R_n) , a constant phase element (CPE) represents the double-layer capacitance and the charge transfer resistance (R_{CT}) for faradaic currents, the superposition of the circuit elements X_1 , G_1 , X_2 , and G_2 represents the intermediate adsorption of anions on the electrode surface during the alkali metal cation insertion process. This physical model describes the so-called "three-step mechanism" of intercalation, which will be briefly introduced in the following. In short, the quick electron transfer on Fe^{II/III} results in the appearance of uncompensated surface charges due to the considerably slower extraction or insertion of sodium from or into the crystal structure. This excess surface charge is compensated by the intermediate adsorption of the highly mobile electrolyte anions on the electrode surface. $^{30-32,55}$ By elaborating the respective kinetic steps of the described interconnected quasireversible processes, the faradaic impedance for the (de)intercalation reaction can be modeled as

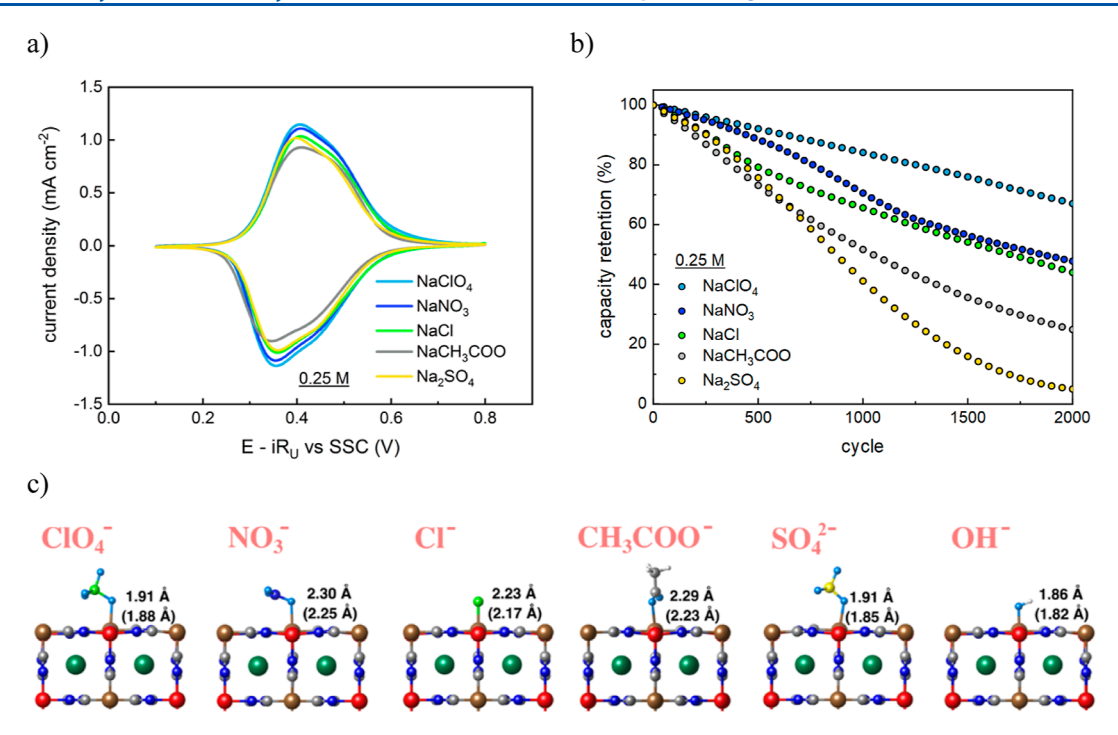


Figure 5. (a) Cyclic voltammograms (50 mV/s) and (b) cycling stability (galvanostatic oxidation and reduction at a rate of 300 C) of NiHCF recorded in 0.25 M Na⁺ electrolytes with varying anion species. (c) DFT optimized structures of a series of anions adsorbed on Fe surface sites of the NiHCF surface along with the Fe–O and Fe–Cl distances. The values are for the fully intercalated and 50% deintercalated (in parentheses) cases. The corresponding adsorption energies are presented in Table 1.

$$\tilde{Z} = R_{ct} + \frac{1}{j\omega G_1 + \frac{1}{X_1 + \frac{1}{j\omega G_2 + \frac{1}{X_2}}}}$$
(3)

The parameters G_1 , G_2 , X_1 , and X_2 are formed by combinations of the complex kinetic parameters of the charge transfer and individual ad/desorption steps associated with the three-step mechanism. Importantly, these parameters can take on both positive and negative values. For a more detailed derivation of the general impedance model for faradaic reactions involving surface adsorbed species, the reader is referred to ref 56.

From Figure 4b, it is apparent that the nature of the anions has, as expected, no significant impact on the charge transfer resistance and thereby the corresponding rate constants of the redox reaction. In contrast, the model elements G_1 and X_1 , which represent the anion adsorption, strongly deviate among the different anions (Figure 4c). From this, we can conclude that the complex interfacial mechanism of alkali metal cation intercalation strongly depends on the respective adsorption affinity of the involved anions. The different ionic conductivities of the salt solutions are represented by the varying uncompensated resistance values (Figure 4d), which are nevertheless in a comparable range.

Following this argumentation, the anion nature should determine the electrochemical performance of PBA electrodes. Figure 5a shows the CVs of NiHCF in 0.25 M Na⁺ electrolytes with ClO₄⁻, NO₃⁻, Cl⁻, CH₃COO⁻, and SO₄²⁻ as the respective anionic species. The potential was corrected for the uncompensated resistance to eliminate any effects stemming from the different ionic conductivities of the solutions. Apparently, the peak shape and position are highly symmetric in all cases and remain unaffected by the present anion. Furthermore, the apparent molar mass of the

intercalating species was determined to be very close to the expected 22.99 g mol⁻¹ for all investigated electrolytes, showing that only sodium is inserted into the host structure (see Figure S6). From the consistently reversible CV curves, it can be concluded that all the tested anionic species effectively compensate for the intermediate excess surface charges during the redox process and that the corresponding adsorption and desorption steps proceed fast enough to not be rate limiting. While this process is supposed to be fully reversible in theory, we observed a significant impact from the involved anion on the electrode stability in our previous study.²⁹

To correlate the degradation rates to the specific anions, we repetitively cycled NiHCF thin-film model electrodes in equally concentrated Na $^+$ electrolytes with comparable neutral pH = 5.7–6.2 (see Table S1), as shown in Figure 5b. The electrode stability was found to decrease in the order of $ClO_4^- > NO_3^- > Cl^- > CH_3COO^- > SO_4^{2-}$, with the capacity retention after 2000 cycles ranging from 67% for perchlorate to only 5% for sulfate. This finding strongly indicates the detrimental effect of some anions and their notable role in promoting electrode dissolution. The order of electrode stability as a function of the involved anion is also in great agreement with previous findings for other PBA materials, namely, NaIn[Fe(CN) $_6$] and $K_2Cr[Fe(CN)<math>_6$]. 57,58

Hypothesizing that the degradation process is initiated by the adsorption of anions from the electrolyte on the metal centers of the NiHCF surface, the adsorption strength and, therefore, the impact of the individual anions should differ considering their distinct geometry, size, charge density, and polarity. To quantify this effect, we examine the adsorption energetics for ClO₄⁻, NO₃⁻, Cl⁻, CH₃COO⁻, SO₄²⁻, and OH⁻. Table 1 lists the computed binding energies for the anions adsorbed at the Fe and Ni surface sites of NiHCF. It is seen that the surface affinity for anions is very strong, assuming

Table 1. DFT Computed Adsorption Energies $(E_{\rm ads})$ for a Series of Electrolyte Anions Adsorbed Over Fe and Ni Surface Sites of Intercalated and 50% Deintercalated NiHCF^a

	intercalated		50% deintercalated	
adsorbate	E _{ads} (Fe), eV	E _{ads} (Ni), eV	E _{ads} (Fe), eV	E _{ads} (Ni), eV
OH-	-2.87	-1.41	-2.91	-1.58
Cl ⁻	-2.73	-2.04	-2.52	-1.74
SO ₄ ²⁻	-3.54	-1.84	-3.55	-2.49
ClO ₄ ⁻	-2.65	-2.35	-2.47	-2.25
NO_3^-	-1.29	-1.35	-1.57	-1.23
CH ₃ COO ⁻	-1.89	-1.26	-1.57	-1.28

^aThe corresponding distances between the adsorbates and the surface metal centers are provided in Figure 5c.

specific adsorption with preferential binding to Fe centers in both intercalated and deintercalated NiHCF. To confirm that these results do not depend on a particular choice of the U values in our computational scheme, we also ran a series of plain DFT calculations (see Table S2). It appears striking to see that even perchlorate, which is known as a weak adsorbate on metals,⁵⁹ yields considerably high adsorption energies when adsorbed over Fe. Figure 5c shows the atomic configurations of the anions adsorbed on the Fe-sites of the NiHCF surface. It can be observed that the stronger adsorbed anions (SO₄²⁻ and OH-) are characterized by shorter interfacial distances than the weaker adsorbed species. Also, the distances are decreased upon deintercalation, in agreement with the overall more positive charge on the host Fe-sites after Na removal (see Table S3). Endorsing our experimental studies, these computational results support the proposed mechanism of anions dictating the kinetics of the interfacial charge and mass transport by adsorption on the electrode surface during (de)intercalation of alkali metal cations in PBAs.^{30–3}

It is also seen from Table 1 that $SO_4^{\ 2-}$ and OH^- anions are characterized by the strongest and CH₃COO⁻, NO₃⁻, and ClO₄ by the weakest adsorption to the NiHCF surface. The calculated adsorption energetics appears to qualitatively correlate with the decreasing stability of NiHCF from the perchlorate to sulfate electrolytes upon cycling. Furthermore, the strong interaction of OH- with the electrode material reflects its fast deterioration in the presence of hydroxide. We, therefore, reason that the low stability of PBAs in high pH media, as well as in the presence of some anionic species in the solution, can be described by a generalized degradation mechanism involving the specific adsorption of anions. The exact dissolution pathways of the specific electrode constituents are certainly too complicated to be entirely unveiled by our simplified approach, but it clearly identifies anion attack to catalyze the degradation process via specific adsorption and subsequent metal extraction by breaking the lattice bonds. Considering the obtained strong (chemi)/adsorption energies in the order of 2-3.5 eV, ligand exchange leading to the formation and dissolution of, for example, [Fe^{III}(CN)₅OH]³⁻ in the alkaline case cannot be excluded.

However, these DFT results cannot explain the experimentally observed low stability of NiHCF in 0.25 M sodium acetate, as one should in fact expect the slowest degradation rate according to the weak anion adsorption in this case. We suppose that the unexpected detrimental role of CH_3COO^- is related to its considerably higher basic strength (p $K_b = 9.2$) compared to the other investigated anions (see Table S4).

Even though the sodium acetate electrolyte was adjusted to a neutral pH = 6.2, this only reflects an overall statistical quantity. On a molecular level, hydrolysis due to deprotonation of H₂O and subsequent CH₃COOH formation will result in the local appearance of free OH-. This in turn accelerates the degradation of the electrode if the process occurs close to its surface. In contrast to the pure NaOH case, this will not lead to the formation of NiO_x (as it is not stable at medium pH) but to the dissolution of active material. Extrapolating these findings, low stability of PBAs in electrolytes involving other (carboxylic) anions corresponding to weak acids should be expected. Furthermore, this argument allows for the explanation of the previously published low stability observed for PBA electrodes in 1 M Mg(ClO₄)₂ solutions.⁶² Besides Mg²⁺, the initial dissolution of NiHCF electrodes was also observed in other divalent metal nitrate electrolytes (Ca²⁺ and Sr²⁺).⁶³ Assuming a similar mechanism, local hydrolysis and X(OH), precipitation (with X = Mg, Ca, and Sr) might result in free H₃O⁺, which can in turn initiate the acidic degradation pathway. Other authors discussed the substitution of lattice Ni(II) by intercalated divalent cations like Mg²⁺, which was assumed to result in the collapse of the framework.⁶⁴ It should, however, be mentioned that the coinsertion of H₃O⁺ cannot be ruled out in divalent cation solutions. 63,65 In contrast to the mixed H₃O⁺/Na⁺ electrolyte, we expect that H₃O⁺ is a preferred intercalate over Mg2+ due to the selectivity of PBAs favoring the insertion of low hydration energy/small radius species over large divalent cations. 47,48 Further research will be necessary to assess the impact of different degradation pathways in the case of PBAs in divalent cation solutions.

Lastly, we investigate the effect of the electrolyte concentration on electrode stability. It has been shown in previous works on PBAs that the dissolution of active material can be suppressed by increasing the concentration of the electrolyte toward the so-called water-in-salt electrolytes. Anaclo₄ has proven to be a promising candidate for this approach as concentrations beyond 10 M are feasible for this salt. Figure 6 shows the stability of NiHCF electrodes in varying concentrations from 0.25 to 8 M NaClo₄. The stability slightly decreases when raising the concentration from 0.25 to 1 M, while a significant stabilization of the material can be observed above 2 M with almost no degradation for an 8 M

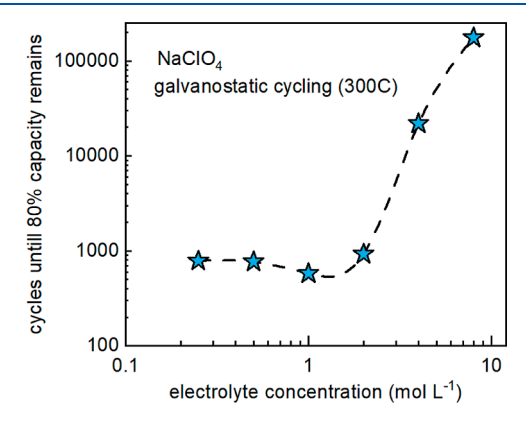


Figure 6. Stability of NiHCF in varying concentrations of NaClO₄ during galvanostatic cycling (300 C). The data points show the number of cycles after a loss of 20% capacity. For the 4 and 8 M solutions, the stability was extrapolated based on the measured capacity losses of 2.6% after 2840 cycles and 1.2% after 10,500 cycles. 29 The dashed line serves as a guide to the eye.

NaClO₄ solution. For the superconcentrated electrolytes, the material hydrolysis is effectively suppressed through the absence of free water molecules, as these are excessively incorporated into the ions' solvation shells due to the strong hydration of the salt. In fact, only a very few water molecules exist per one sodium perchlorate molecule causing a vanishing uptake capability for dissolved electrode constituents. Furthermore, the sluggish diffusion dynamics for dissolved electrode constituents in the electrolyte bulk strongly inhibit electrode degradation in such water-in-salt systems. ⁶⁹ For the low-to-medium concentrated solutions, we assign the slight decrease in the stability to the effect of the ClO₄⁻ anion. Even though this species was found to adsorb on the electrode surface only weakly, its increased activity at higher concentrations could lead to a stronger degradation of the active material. However, beyond a concentration of 2 M, the stabilizing crowding effect of the electrolyte prevails.

CONCLUSIONS

In this work, the governing mechanisms driving the degradation of model Na₂Ni[Fe(CN)₆] electrodes based on the electrolyte composition were elucidated by a combined experimental and theoretical approach. DFT calculations for the anions commonly used in electrochemical systems showed that the NiHCF surface has a significant affinity for anion adsorption with binding energies up to ~3.5 eV. This finding emphasizes a non-negligible role of anion-specific adsorption in the complex mechanism of interfacial mass and charge transfer during the intercalation of alkali metal cations. It is shown that the surface Fe-sites are more favorable for anion adsorption than Ni-sites, forming the following trend for the adsorption strength of anions on Fe (surface layer atoms): $SO_4^{2^-} > OH^- > Cl^- > ClO_4^- > CH_3COO^- > NO_3^-$. The anion adsorption characteristics allow us to explain the drastic differences in the stability of PBA electrodes, confirming the experimentally determined higher stability in the presence of weakly adsorbing anions like ClO₄⁻ and NO₃⁻ compared to the strongly adsorbing SO₄²⁻ and OH⁻. Considering the special role of hydroxide on PBA decomposition, the respective basic strength of the anions also has to be taken into account, excluding the acetate anion from stable electrode cycling. Whereas benign acidification (pH $\sim 2-3$) of the electrolyte generally helps to increase the stability due to the decreased OH⁻ activity, an overwhelming availability and intercalation of H_3O^+ cause a fast deterioration of the Ni-[N \equiv C-Fe] bond due to protonation of the N-sites within the crystal structure and subsequent electrode dissolution.

We point out, however, that it is not straightforward to predict the stability of PBAs in aqueous environments by a single generalized mechanism. Overall, the material stability is determined by a complex interplay of competing processes involving anion attack via strong adsorption on the electrified interface, specifically OH⁻-induced hydrolysis, and protonation of the CN group in the presence of hydronium. Therefore, the exact composition of the electrolyte should be carefully considered for achieving a long material lifetime as the solution pH, salt concentration, and the involved anion determine its resistance against degradation. These findings should be of great importance in optimizing electrochemical systems based on PBA materials, interpreting experimental results, and elucidating the advanced models of the electrified PBA/electrolyte interfaces.

ASSOCIATED CONTENT

Supporting Information

The Supporting Information is available free of charge at https://pubs.acs.org/doi/10.1021/acs.jpcc.2c08222.

Used sodium salt solutions with suppliers and respective pH values; computed anion binding energies via plain DFT calculations; computed local charge on Fe- and Nisites; list of acid and basic strength of investigated species; characterization of NiHCF in 0.25 M H₂SO₄, 0.1 M NaOH, and a mixed 0.25 M HClO₄ and NaClO₄ (1:1) electrolytes; apparent molar mass of the (de)-intercalating species during cycling of NiHCF in different Na⁺ electrolytes; and Kramers–Kronig check for the impedance spectra of NiHCF (PDF)

AUTHOR INFORMATION

Corresponding Authors

Aliaksandr S. Bandarenka — Physics of Energy Conversion and Storage, Physik-Department, Technische Universität München, Garching bei München 85748, Germany; orcid.org/0000-0002-5970-4315; Email: bandarenka@ph.tum.de

Vitaly Alexandrov — Department of Chemical and Biomolecular Engineering and Nebraska Center for Materials and Nanoscience, University of Nebraska—Lincoln, Lincoln, Nebraska 68588, United States; orcid.org/0000-0003-2063-6914; Email: valexandrov2@unl.edu

Authors

Xaver Lamprecht – Physics of Energy Conversion and Storage, Physik-Department, Technische Universität München, Garching bei München 85748, Germany

Iman Evazzade – Department of Chemical and Biomolecular Engineering and Nebraska Center for Materials and Nanoscience, University of Nebraska–Lincoln, Lincoln, Nebraska 68588, United States

Iago Ungerer – Physics of Energy Conversion and Storage, Physik-Department, Technische Universität München, Garching bei München 85748, Germany

Ludek Hromadko – Central European Institute of Technology, Brno University of Technology, Brno 61200, Czech Republic; Center of Materials and Nanotechnologies, Faculty of Chemical Technology, University of Pardubice, Pardubice 53002, Czech Republic

Jan M. Macak – Central European Institute of Technology, Brno University of Technology, Brno 61200, Czech Republic; Center of Materials and Nanotechnologies, Faculty of Chemical Technology, University of Pardubice, Pardubice 53002, Czech Republic

Complete contact information is available at: https://pubs.acs.org/10.1021/acs.jpcc.2c08222

Notes

The authors declare no competing financial interest.

ACKNOWLEDGMENTS

We want to thank the German Research Foundation (DFG) under Germany's excellence strategy—EXC 2089/1-390776260, Germany's excellence cluster "e-conversion". We acknowledge funding support from the National Science Foundation (NSF) through the CBET-1929810 award. This research used the Extreme Science and Engineering Discovery

Environment (XSEDE), which is supported by NSF grant number ACI-1548562, as well as the Leibniz Supercomputing Center (LRZ). XRD and SEM analyses were carried out with the support of the CEMNAT Research Infrastructure funded by the Ministry of Education, Youth and Sports of the Czech Republic (projects LM2018103)

REFERENCES

- (1) Han, J.; Varzi, A.; Passerini, S. The Emergence of Aqueous Ammonium-Ion Batteries. *Angew. Chem., Int. Ed.* **2022**, *61*, No. e202115046.
- (2) Hurlbutt, K.; Wheeler, S.; Capone, I.; Pasta, M. Prussian Blue Analogs as Battery Materials. *Joule* **2018**, *2*, 1950–1960.
- (3) Xie, B.; Sun, B.; Gao, T.; Ma, Y.; Yin, G.; Zuo, P. Recent progress of Prussian blue analogues as cathode materials for nonaqueous sodium-ion batteries. *Coord. Chem. Rev.* **2022**, *460*, 214478.
- (4) Wang, B.; Han, Y.; Wang, X.; Bahlawane, N.; Pan, H.; Yan, M.; Jiang, Y. Prussian Blue Analogs for Rechargeable Batteries. *iScience* **2018**, *3*, 110–133.
- (5) Yi, H.; Qin, R.; Ding, S.; Wang, Y.; Li, S.; Zhao, Q.; Pan, F. Structure and properties of prussian blue analogues in energy storage and conversion applications. *Adv. Funct. Mater.* **2021**, *31*, 2006970.
- (6) Karyakin, A. A. Prussian blue and its analogues: electrochemistry and analytical applications. *Electroanalysis* **2001**, *13*, 813–819.
- (7) Avila, Y.; Acevedo-Peña, P.; Reguera, L.; Reguera, E. Recent progress in transition metal hexacyanometallates: From structure to properties and functionality. *Coord. Chem. Rev.* **2022**, *453*, 214274.
- (8) Matos-Peralta, Y.; Antuch, M. Prussian blue and its analogs as appealing materials for electrochemical sensing and biosensing. *J. Electrochem. Soc.* **2019**, *167*, 037510.
- (9) Chen, S. M.; Liou, C. Y.; Thangamuthu, R. Preparation and characterization of mixed-valent nickel oxide/nickel hexacyanoferrate hybrid films and their electrocatalytic properties. *Electroanalysis* **2007**, 19, 2457–2464.
- (10) Su, X.; Wang, Y.; Zhou, J.; Gu, X.; Li, J.; Zhang, S. Operando spectroscopic identification of active sites in NiFe Prussian Blue Analogues as electrocatalysts: activation of oxygen atoms for oxygen evolution reaction. *J. Am. Chem. Soc.* **2018**, *140*, 11286–11292.
- (11) Zhang, H.; Li, P.; Chen, S.; Xie, F.; Riley, D. J. Anodic transformation of a core-shell Prussian Blue Analogue to a bifunctional electrocatalyst for water splitting. *Adv. Funct. Mater.* **2021**, *31*, 2106835.
- (12) Rassat, S. D.; Sukamto, J. H.; Orth, R. J.; Lilga, M. A.; Hallen, R. T. Development of an electrically switched ion exchange process for selective ion separations. *Sep. Purif. Technol.* **1999**, *15*, 207–222.
- (13) Kim, T.; Gorski, C. A.; Logan, B. E. Ammonium removal from domestic wastewater using selective battery electrodes. *Environ. Sci. Technol. Lett.* **2018**, *5*, 578–583.
- (14) Reale, E. R.; Regenwetter, L.; Agrawal, A.; Dardón, B.; Dicola, N.; Sanagala, S.; Smith, K. C. Low porosity, high areal-capacity Prussian blue analogue electrodes enhance salt removal and thermodynamic efficiency in symmetric faradaic deionization with automated fluid control. *Water Res.: X* **2021**, *13*, 100116.
- (15) Shibata, T.; Moritomo, Y. Quick response of all solid electrochromic device. *Appl. Phys. Express* **2009**, *2*, 105502.
- (16) Assis, L. M. N.; Leones, R.; Kanicki, J.; Pawlicka, A.; Silva, M. M. Prussian blue for electrochromic devices. *J. Electroanal. Chem.* **2016**, 777, 33–39.
- (17) Cattermull, J.; Pasta, M.; Goodwin, A. L. Structural complexity in Prussian blue analogues. *Mater. Horiz.* **2021**, *8*, 3178–3186.
- (18) Boström, H. L. B.; Brant, W. R. Octahedral tilting in Prussian blue analogues. J. Mater. Chem. C 2022, 10, 13690–13699.
- (19) Zhang, W.; Wu, Y.; Li, Z.; Dong, H.; Zhang, Y.; Gu, N.. *Nanozymology*; Springer: Singapore, 2020; pp 141–170.
- (20) Yang, Y.; Brownell, C.; Sadrieh, N.; May, J.; Del Grosso, A.; Place, D.; Leutzinger, E.; Duffy, E.; He, R.; Houn, F.; et al.

- Quantitative measurement of cyanide released from Prussian Blue. *Environ. Sci. Technol. Lett.* **2007**, *45*, 776–781.
- (21) Zhang, W.; Zhao, Y.; Malgras, V.; Ji, Q.; Jiang, D.; Qi, R.; Ariga, K.; Yamauchi, Y.; Liu, J.; Jiang, M.; et al. Synthesis of monocrystalline nanoframes of prussian blue analogues by controlled preferential etching. *Angew. Chem., Int. Ed.* **2016**, *55*, 8228–8234.
- (22) Zhu, Y.; Wang, B.; Gan, Q.; Wang, Y.; Wang, Z.; Xie, J.; Gu, S.; Li, Z.; Li, Y.; Ji, Z.; et al. Selective edge etching to improve the rate capability of Prussian blue analogues for sodium ion batteries. *Inorg. Chem. Front.* **2019**, *6*, 1361–1366.
- (23) Hu, M.; Furukawa, S.; Ohtani, R.; Sukegawa, H.; Nemoto, Y.; Reboul, J.; Kitagawa, S.; Yamauchi, Y. Synthesis of Prussian blue nanoparticles with a hollow interior by controlled chemical etching. *Angew. Chem., Int. Ed.* **2012**, *51*, 984–988.
- (24) Hu, M.; Belik, A. A.; Imura, M.; Yamauchi, Y. Tailored design of multiple nanoarchitectures in metal-cyanide hybrid coordination polymers. *J. Am. Chem. Soc.* **2013**, *135*, 384–391.
- (25) Stilwell, D. E.; Park, K. H.; Miles, M. H. Electrochemical studies of the factors influencing the cycle stability of Prussian Blue films. *J. Appl. Electrochem.* **1992**, *22*, 325–331.
- (26) Mimura, H.; Lehto, J.; Harjula, R. Chemical and thermal stability of potassium nickel hexacyanoferrate(II). *J. Nucl. Sci. Technol.* **1997**, 34, 582–587.
- (27) Marzak, P.; Yun, J.; Dorsel, A.; Kriele, A.; Gilles, R.; Schneider, O.; Bandarenka, A. S. Electrodeposited $Na_2Ni[Fe(CN)_6]$ thin-film cathodes exposed to simulated aqueous Na-ion battery conditions. *J. Phys. Chem. C* **2018**, *122*, 8760–8768.
- (28) Cataldi, T. R.; Guascito, R.; Maria Salvi, A. M. XPS study and electrochemical behaviour of the nickel hexacyanoferrate film electrode upon treatment in alkaline solutions. *J. Electroanal. Chem.* **1996**, *417*, 83–88.
- (29) Lamprecht, X.; Speck, F.; Marzak, P.; Cherevko, S.; Bandarenka, A. S. Electrolyte effects on the stabilization of Prussian blue analog electrodes in aqueous sodium-ion batteries. *ACS Appl. Mater. Interfaces* **2022**, *14*, 3515–3525.
- (30) Scieszka, D.; Sohr, C.; Scheibenbogen, P.; Marzak, P.; Yun, J.; Liang, Y.; Fichtner, J.; Bandarenka, A. S. Multiple potentials of maximum entropy of a Na₂Co[Fe(CN)₆] battery electrode material: does the electrolyte composition control the interface? *ACS Appl. Mater. Interfaces* **2018**, *10*, 21688–21695.
- (31) Ventosa, E.; Paulitsch, B.; Marzak, P.; Yun, J.; Schiegg, F.; Quast, T.; Bandarenka, A. S. The mechanism of the interfacial charge and mass transfer during intercalation of alkali metal cations. *Adv. Sci.* **2016**, *3*, 1600211.
- (32) Yun, J.; Pfisterer, J.; Bandarenka, A. S. How simple are the models of Na-intercalation in aqueous media? *Energy Environ. Sci.* **2016**, *9*, 955–961.
- (33) Bandarenka, A. S. Development of hybrid algorithms for EIS data fitting. Lect. Notes Impedance Spectrosc. 2013, 4, 29–36.
- (34) Momma, K.; Izumi, F. VESTA 3 for three-dimensional visualization of crystal, volumetric and morphology data. *J. Appl. Crystallogr.* **2011**, *44*, 1272–1276.
- (35) Kresse, G.; Furthmüller, J. Efficient iterative schemes for ab initio total-energy calculations using a plane-wave basis set. *Phys. Rev. B: Condens. Matter Mater. Phys.* **1996**, *54*, 11169–11186.
- (36) Kresse, G.; Furthmüller, J. Efficiency of ab-initio total energy calculations for metals and semiconductors using a plane-wave basis set. *Comput. Mater. Sci.* **1996**, *6*, 15–50.
- (37) Perdew, P.; Burke, K.; Ernzerhof, M. Generalized gradient approximation made simple. *Phys. Rev. Lett.* **1996**, *77*, 3865–3868.
- (38) Zhang, Y.; Yang, W. Comment on "Generalized gradient approximation made simple". *Phys. Rev. Lett.* **1998**, *80*, 890.
- (39) Grimme, S.; Antony, J.; Ehrlich, S.; Krieg, H. A consistent and accurate ab initio parametrization of density functional dispersion correction (DFT-D) for the 94 elements H-Pu. *J. Chem. Phys.* **2010**, *132*, 154104.
- (40) Grimme, S.; Ehrlich, S.; Goerigk, L. Effect of the damping function in dispersion corrected density functional theory. *J. Comput. Chem.* **2011**, 32, 1456–1465.

- (41) Blöchl, P. E. Projector augmented-wave method. *Phys. Rev. B: Condens. Matter Mater. Phys.* **1994**, *50*, 17953–17978.
- (42) Gerber, S. J.; Erasmus, E. Electronic effects of metal hexacyanoferrates: An XPS and FTIR study. *Mater. Chem. Phys.* **2018**, 203, 73–81.
- (43) Bácskai, J.; Martinusz, K.; Czirók, E.; Inzelt, G.; Kulesza, P. J.; Malik, M. A. Polynuclear nickel hexacyanoferrates: monitoring of film growth and hydrated counter-cation flux/storage during redox reactions. *J. Electroanal. Chem.* **1995**, 385, 241–248.
- (44) Chen, W.; Tang, J.; Xia, X. H. Composition and shape control in the construction of functional nickel hexacyanoferrate nanointerfaces. *J. Phys. Chem. C* **2009**, *113*, 21577–21581.
- (45) Hao, X.; Yan, T.; Wang, Z.; Liu, S.; Liang, Z.; Shen, Y.; Pritzker, M. Unipolar pulse electrodeposition of nickel hexacyanoferrate thin films with controllable structure on platinum substrates. *Thin Solid Films* **2012**, *520*, 2438–2448.
- (46) Paulitsch, B.; Yun, J.; Bandarenka, A. S. Electrodeposited $Na_2VO_x[Fe(CN)_6]$ films as a cathode material for aqueous Na-ion batteries. *ACS Appl. Mater. Interfaces* **2017**, *9*, 8107–8112.
- (47) Lee, H. W.; Pasta, M.; Wang, R. Y.; Ruffo, R.; Cui, Y. Effect of the alkali insertion ion on the electrochemical properties of nickel hexacyanoferrate electrodes. *Faraday Discuss.* **2014**, *176*, 69–81.
- (48) Gamaethiralalage, J. G.; Singh, K.; Sahin, S.; Yoon, J.; Elimelech, M.; Suss, M. E.; Liang, P.; Biesheuvel, P. M.; Zornitta, R. L.; de Smet, L. C. P. M. Recent advances in ion selectivity with capacitive deionization. *Energy Environ. Sci.* **2021**, *14*, 1095–1120.
- (49) Erinmwingbovo, C.; Palagonia, M. S.; Brogioli, D.; La Mantia, F. Intercalation into a Prussian blue derivative from solutions containing two species of cations. *ChemPhysChem* **2017**, *18*, 917–925.
- (50) Wu, X.; Hong, J. J.; Shin, W.; Ma, L.; Liu, T.; Bi, X.; Yuan, Y.; Qi, Y.; Surta, T. W.; Huang, X.; et al. Diffusion-free Grotthuss topochemistry for high-rate and long-life proton batteries. *Nat. Energy* **2019**, *4*, 123–130.
- (51) Wessells, C. D.; Peddada, S. V.; Huggins, R. A.; Cui, Y. Nickel hexacyanoferrate nanoparticle electrodes for aqueous sodium and potassium ion batteries. *Nano Lett.* **2011**, *11*, 5421–5425.
- (52) Wessells, C. D.; Huggins, R. A.; Cui, Y. Copper hexacyanoferrate battery electrodes with long cycle life and high power. *Nat. Commun.* **2011**, *2*, 550.
- (53) Doménech, A.; Montoya, N.; Scholz, F. Estimation of individual Gibbs energies of cation transfer employing the insertion electrochemistry of solid Prussian blue. *J. Electroanal. Chem.* **2011**, 657, 117–122.
- (54) Dinkelacker, F.; Marzak, P.; Yun, J.; Liang, Y.; Bandarenka, A. S. Multistage mechanism of lithium intercalation into graphite anodes in the presence of the solid electrolyte interface. *ACS Appl. Mater. Interfaces* **2018**, *10*, 14063–14069.
- (55) Gaddam, R. R.; Katzenmeier, L.; Lamprecht, X.; Bandarenka, A. S. Review on physical impedance models in modern battery research. *Phys. Chem. Chem. Phys.* **2021**, 23, 12926–12944.
- (56) Lasia, A.Electrochemical Impedance Spectroscopy and its Applications; Springer: New York, 2014; Chapter 5.
- (57) Lamprecht, X.; Marzak, P.; Wieczorek, A.; Thomsen, N.; Kim, J.; Garlyyev, B.; Liang, Y.; Bandarenka, A. S.; Yun, J. High voltage and superior cyclability of indium hexacyanoferrate cathodes for aqueous Na-ion batteries enabled by superconcentrated NaClO₄ electrolytes. *Energy Adv.* **2022**, *1*, 623–631.
- (58) Bors, R.; Yun, J.; Marzak, P.; Fichtner, J.; Scieszka, D.; Bandarenka, A. S. Chromium(II) hexacyanoferrate-based thin films as a material for aqueous alkali metal cation batteries. *ACS Omega* **2018**, 3, 5111–5115.
- (59) Kasuya, M.; Sogawa, T.; Masuda, T.; Kamijo, T.; Uosaki, K.; Kurihara, K. Anion adsorption on gold electrodes studied by electrochemical surface forces measurement. *J. Phys. Chem. C* **2016**, 120, 15986–15992.
- (60) Trummal, A.; Lipping, L.; Kaljurand, I.; Koppel, I. A.; Leito, I. Acidity of strong acids in water and dimethyl sulfoxide. *J. Phys. Chem.* A **2016**, *120*, 3663–3669.

- (61) Dean, J.Lange's Handbook of Chemistry, 15th ed.; McGraw-Hill, 1999; Section 8.
- (62) Marzak, P.; Kosiahn, M.; Yun, J.; Bandarenka, A. S. Intercalation of Mg²⁺ into electrodeposited Prussian Blue Analogue thin films from aqueous electrolytes. *Electrochim. Acta* **2019**, 307, 157–163.
- (63) Wang, R. Y.; Wessells, C. D.; Huggins, R. A.; Cui, Y. Highly reversible open framework nanoscale electrodes for divalent ion batteries. *Nano Lett.* **2013**, *13*, 5748–5752.
- (64) Shrivastava, A.; Liu, S.; Smith, K. C. Linking capacity loss and retention of nickel hexacyanoferrate to a two-site intercalation mechanism for aqueous Mg²⁺ and Ca²⁺ ions. *Phys. Chem. Chem. Phys.* **2019**, *21*, 20177–20188.
- (65) Komayko, A. I.; Ryazantsev, S. V.; Trussov, I. A.; Arkharova, N. A.; Presnov, D. E.; Levin, E. E.; Nikitina, V. A. The Misconception of Mg²⁺ Insertion into Prussian Blue Analogue Structures from Aqueous Solution. *ChemSusChem* **2021**, *14*, 1574–1585.
- (66) Pasta, M.; Wessells, C. D.; Liu, N.; Nelson, J.; McDowell, M. T.; Huggins, R. A.; Toney, M. F.; Cui, Y. Full open-framework batteries for stationary energy storage. *Nat. Commun.* **2014**, *5*, 3007.
- (67) Reber, D.; Grissa, R.; Becker, M.; Kühnel, R. S.; Battaglia, C. Anion selection criteria for water-in-salt electrolytes. *Adv. Energy Mater.* **2021**, *11*, 2002913.
- (68) Tomiyasu, H.; Shikata, H.; Takao, K.; Asanuma, N.; Taruta, S.; Park, Y. Y. An aqueous electrolyte of the widest potential window and its superior capability for capacitors. *Sci. Rep.* **2017**, *7*, 45048.
- (69) Chen, L.; Sun, W.; Xu, K.; Dong, Q.; Zheng, L.; Wang, J.; Lu, D.; Shen, Y.; Zhang, J.; Fu, H.; et al. How Prussian Blue Analogues can be stable in concentrated aqueous electrolytes. *ACS Energy Lett.* **2022**, *7*, 1672–1678.

☐ Recommended by ACS

Ball Milling-Enabled Fe^{2.4+} to Fe³⁺ Redox Reaction in Prussian Blue Materials for Long-Life Aqueous Sodium-Ion Batteries

Marcos Lucero, Zhenxing Feng, et al.

JULY 23, 2023

ACS APPLIED MATERIALS & INTERFACES

READ 🗹

Fast-Charging Capability of Thin-Film Prussian Blue Analogue Electrodes for Aqueous Sodium-Ion Batteries

Xaver Lamprecht, Aliaksandr S. Bandarenka, et al.

MAY 05, 2023

ACS APPLIED MATERIALS & INTERFACES

READ 🗹

Fluffy-Like Cation-Exchanged Prussian Blue Analogues for Sodium-Ion Battery Cathodes

Yaozong Zhou, Man Xie, et al.

JULY 06, 2022

ACS APPLIED MATERIALS & INTERFACES

READ 🗹

Continuous Production of High-Capacity Iron-Based Prussian Blue Sodium-Ion Cathode Materials Using a Rotor-Stator Spinning Disk Reactor

Pan Zhu, Yang Jin, et al.

MAY 05, 2023

ACS APPLIED ENERGY MATERIALS

READ 🗹

Get More Suggestions >